

A Long-term study of three rotating radio transients

B. Bhattacharyya,^{1*} A. G. Lyne,² B. W. Stappers,² P. Weltevrede,² E. F. Keane,^{2,3}
M. A. McLaughlin,^{4,5} M. Kramer,^{2,6} C. Jordan,² C. Bassa⁷

¹ National Centre for Radio Astrophysics, Tata Institute of Fundamental Research, Pune 411 007, India

² Jodrell Bank Centre for Astrophysics, School of Physics and Astronomy, The University of Manchester, Manchester M13 9PL, UK

³ SKA Organisation, Jodrell Bank Observatory, SK11 9DL, UK

⁴ Department of Physics & Astronomy, West Virginia University, Morgantown, WV 26506, US

⁵ Center for Gravitational Waves and Cosmology, West Virginia University, Chestnut Ridge Research Building, Morgantown, WV 26505

⁶ Max-Planck-Institut für Radioastronomie, Auf dem Hügel 69, D-53121 Bonn, Germany

⁷ ASTRON, the Netherlands Institute for Radio Astronomy, Postbus 2, 7990 AA, Dwingeloo, The Netherlands

Accepted XXX. Received YYY; in original form ZZZ

ABSTRACT

We present the longest-term timing study so far of three Rotating Radio Transients (RRATs) – J1819–1458, J1840–1419 and J1913+1330 – performed using the Lovell, Parkes and Green Bank telescopes over the past decade. We study long-term and short-term variations of the pulse emission rate from these RRATs and report a marginal indication of a long-term increase in pulse detection rate over time for PSR J1819–1458 and J1913+1330. For PSR J1913+1330, we also observe a two orders of magnitude variation in the observed pulse detection rates across individual epochs, which may constrain the models explaining the origin of RRAT pulses. PSR J1913+1330 is also observed to exhibit a weak persistent emission mode.

We investigate the post-glitch timing properties of J1819–1458 (the only RRAT for which glitches are observed) and discuss the implications for possible glitch models. Its post-glitch over-recovery of the frequency derivative is magnetar-like and similar behaviour is only observed for two other pulsars, both of which have relatively high magnetic field strengths. Following the over-recovery we also observe that some fraction of the pre-glitch frequency derivative is gradually recovered.

Key words: Stars: pulsar: RRATs :individual: J1819–1458, J1840–1419, J1913+1330

1 INTRODUCTION

Occasional flashes of dispersed radio emission of typically a few milliseconds duration are detected from the Rotating Radio Transients (RRATs; McLaughlin et al. (2006)). Even though the pulses appear randomly, there is a characteristic underlying periodicity associated with the emission detected from the RRATs. Timing studies and multi-wavelength observations have revealed that RRATs are neutron stars, most likely an extreme manifestation of the overall neutron star intermittency spectrum. A decade since their discovery by McLaughlin et al. (2006), there are 112 known RRATs¹ having spin periods ranging from 0.125 s to 7.7 s and dispersion measures ranging from 9.2 pc cm⁻³ to 554.9 pc cm⁻³. Measurements of the period derivative exist for only 29 of RRATs, ranging from 5.7×10⁻¹³ to 1.2×10⁻¹⁶ s/s. The pe-

riod and magnetic field strength distributions of the RRATs are skewed to larger values compared to that of the normal pulsars, with some comparable to those of X-ray detected radio-quiet isolated neutron stars and magnetars (Cui et al. 2017). The origin of RRAT emission is not yet known and a number of postulates exist in the literature. To name a few, the pulses observed from RRATs are thought to be associated with, (a) giant pulses from weak pulsars (Knight et al. 2006), (b) a manifestation of extreme nulling of radio pulsars (Redman et al. 2009), (c) created due to the presence of a circumstellar asteroid/radiation belt around the pulsar (Cordes et al. 2008), or (d) from systems similar to PSR B0656+14, for which emission properties would have been similar to the RRATs if this pulsar is placed at a larger distance (Weltevrede et al. 2006). Therefore we do not know if RRATs represent a truly separate population of radio emitting neutron stars like magnetars or isolated neutron stars. Phase-connected timing solutions for RRATs provide timing models with information about the period, period derivative,

* E-mail: bhaswati@ncra.tifr.res.in

¹ <http://astro.phys.wvu.edu/rratalog/>

magnetic field strength and spin down energy rate; enabling us to compare these properties with rest of the neutron star population. Timing solutions are also important to obtain accurate positions which facilitate identification of possible high energy counterparts.

In this paper we present results from long-term monitoring of three RRATs, J1819–1458, J1840–1419 (originally known as J1841–1418) and J1913+1330 (originally known as J1913+1333). This study reports results for regular observations of these RRATs over the past decade and presents the longest time-span investigation of RRATs.

The brightest known RRAT is J1819–1458. This is one of the first RRATs discovered by [McLaughlin et al. \(2006\)](#). It has a wide multi-component profile and is located in the upper right part of the $P - \dot{P}$ diagram, in the same area occupied by the magnetars and high magnetic field pulsars. PSR J1819–1458 is the only RRAT that is also detected in X-rays ([Rea et al. 2009](#)). The detection of an X-ray counterpart with properties similar to those of other neutron stars provides a strong link to relate RRATs with the greater neutron star population. Extended X-ray emission is also detected around PSR J1819–1458 ([Camero-Arranz et al. 2013](#)), which can be interpreted as being a nebula powered by the RRAT. [Dhillon et al. \(2011\)](#) attempted to detect optical emission from simultaneous ULTRACAM on the William Herschel Telescope and Lovell observations, and found no evidence of optical pulses at magnitudes brighter than $i=19.3$ to a 5σ limit. [Karastergiou et al. \(2009\)](#) studied the polarisation properties of J1819–1458 with Parkes at 1420 MHz. The polarisation characteristics and integrated profile resemble those of normal pulsars with average spin-down energy \dot{E} , and a smooth S-shaped swing of polarisation position angle. [Lyne et al. \(2009\)](#) presented a timing analysis of PSR J1819–1458 starting from the discovery observations on 1998 August, followed by 5 years of timing starting in 2003. They reported the detection of two glitches (characterised by sudden jumps in rotational frequency) from this RRAT, having similar magnitude to the glitches observed for radio pulsars and magnetars. So far it is the only RRAT for which glitches are observed. The lack of glitches observed in RRATs can be explained by the fact that they appear to represent a slightly older population of the neutron stars and glitches are generally observed in younger pulsars. Moreover, very few RRATs have timing solutions or even being regularly timed. [Lyne et al. \(2009\)](#) observed atypical post-glitch properties for PSR J1819–1458. The glitches resulted in a long term reduction in the average spin-down rate as opposed to the increase of average spin-down rate generally observed for pulsars.

PSR J1840–1419 was discovered in a re-analysis of the Parkes multi-beam survey ([Keane et al. 2010](#)). [Keane et al. \(2011\)](#) reported its coherent timing solution for the data span from March 2009 to October 2010. [Keane et al. \(2013\)](#) performed X-ray observations of J1840–1419 and calculated a blackbody temperature upper limit, implying that this RRAT is one of the coolest neutron stars known.

PSR J1913+1330 was discovered by [McLaughlin et al. \(2006\)](#). The timing solution of PSR J1913+1330 from January 2004 to April 2009 was presented by [McLaughlin et al. \(2009\)](#). They observed that PSR J1913+1330 has spin properties indistinguishable from the rest of the radio pulsar population.

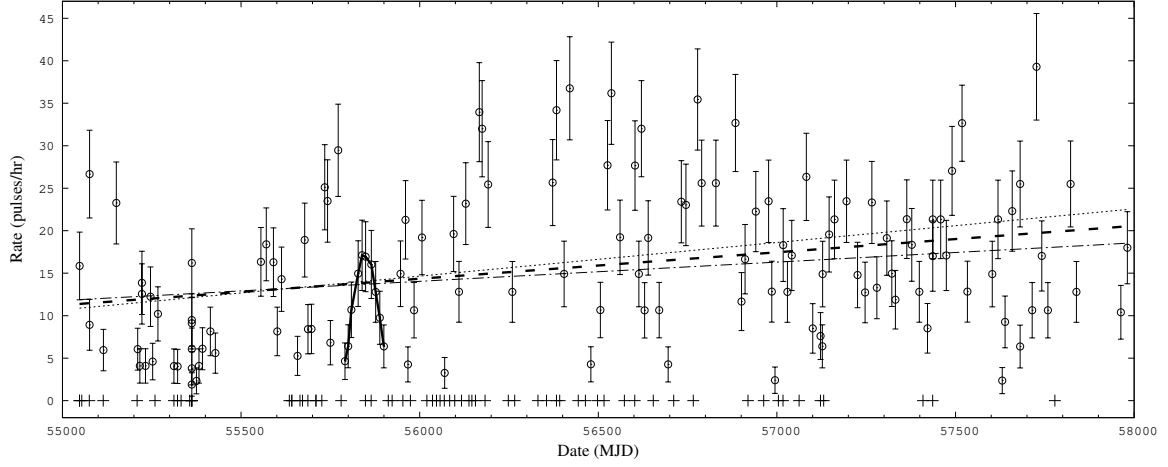
In §2 we describe the observations. In §3.1 we report an investigation of the pulse rate statistics of these three RRATs. §3.2 describes the timing study of PSR J1819–1458. §3.3 and §3.4 details the timing study of PSR J1840–1419 and PSR J1913+1330 respectively. §3.5 presents the detection of a weak emission mode for PSR J1913+1330. In §4 we discuss and summarise the main results from this study.

2 OBSERVATIONS AND ANALYSIS

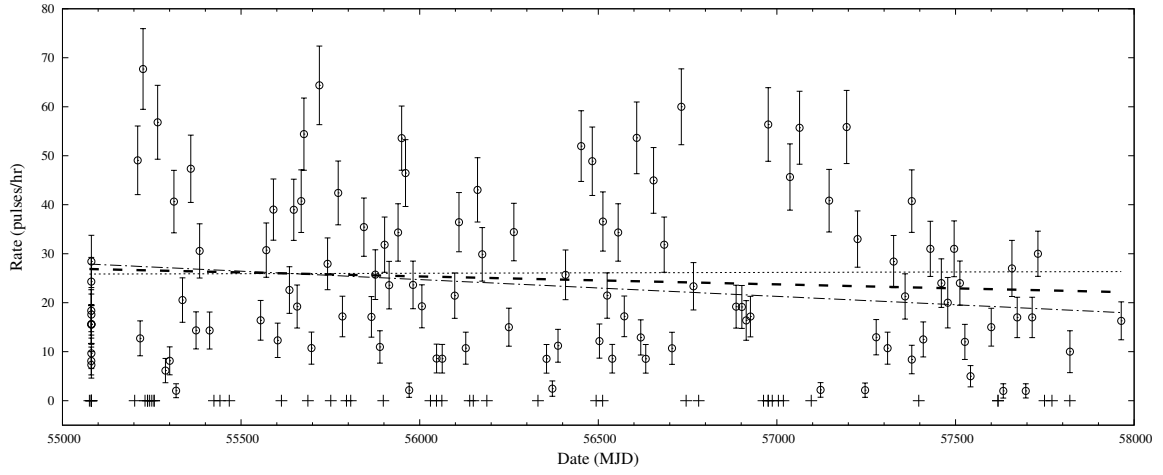
The observations were carried out using the 64-m Parkes Telescope in Australia and 76-m the Lovell telescope at Jodrell Bank in the UK at frequencies of around 1.4 GHz and the 100-m Green Bank Telescope in the USA at 2.2 GHz. The observations up to March 2009 were reported in [Lyne et al. \(2009\)](#) and [McLaughlin et al. \(2009\)](#). Building on these previously reported results, we have observed these pulsars for at least 8 more years with the 76-m Lovell telescope. At the Parkes telescope, dual orthogonal linear polarisations were added to generate total intensity recorded after forming a 512×0.5 MHz filter bank, with sampling resolution of 100 μ s. At the Lovell telescope dual orthogonal circular polarisations were added to generate total intensity. Observations between March 2009 and August 2009 were performed with the analog filterbank backend (AFB) with 64 MHz bandwidth with 100 μ s time resolution. Observations after August 2009 till May 2016 were recorded with the digital backend (DFB) ([Hobbs et al. 2014](#)), with 300 MHz bandwidth and 100 μ s time resolution. Because of the increased bandwidth, the sensitivity of the DFB backend is ~ 2 times greater than that of the AFB backend. The observations were mostly of 30 mins in duration. The data were affected by radio frequency interference (RFI). We masked a standard list of RFI frequency channels for the Lovell telescope coming from known RFI sources, and removed other RFI occurrences by visual inspection.

Pulsar timing is normally performed with times-of-arrival (TOAs) calculated from integrated pulse profiles generated by adding a large number of (typically ~ 1000) single pulses folded with the known pulsar period, to provide increased signal-to-noise and a stable pulse profile. For timing of RRATs, we need to work with individual pulses as opposed to the integrated profiles because of the sporadic nature of their emission. The detected single pulses from RRATs are generally quite strong, with typical peak flux densities of $\sim 10^2 - 10^3$ mJy ([Keane et al. 2011](#)). For the three RRATs studied in this paper, the signal-to-noise ratio of the individual pulses is sufficient to generate TOAs from each pulse. For this purpose we dedispersed the data with a range of dispersion measure (DM) values around the DM of the RRAT and also at a DM of zero. Then we searched for pulses above 5σ from both the time series using the SIGPROC² pulsar data processing package. Results from both the searches are compared and those pulses with stronger detection at the DM of the RRAT than at a DM of zero were considered. We improved the data quality by using zero-DM filtering ([Eatough et al. 2009](#)). Finally visual investigation of

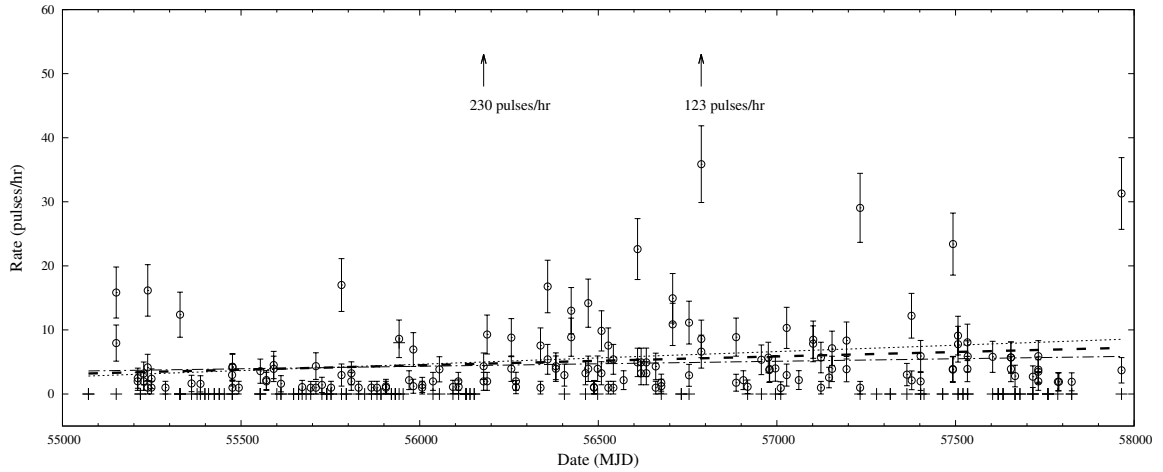
² <http://sigproc.sourceforge.net>



(a) PSR J1819-1458



(b) PSR J1840-1419



(c) PSR J1913+1330

Figure 1. Pulse detection rate at each observing epoch vs the MJD of that epoch, for the RRATs J1819-1458, J1840-1419 and J1913+1330. Statistical error bars for each data rate are plotted (Gehrels et al. 1986). The thick dashed lines are linear fits to the data, while the dotted line and the dash-dot lines represent the 1σ error on the fitted line. Parameters for the fitted straight lines are presented in Table 1. In all the cases the reduced chi-square is much more than unity, indicating inconsistency with a fixed emission rate for these RRATs from day to day. Two epochs with order of magnitude higher detection rates for PSR J1913+1330 are denoted by the upwards arrows. The epochs where no pulses were detected from the RRATs are indicated by '+

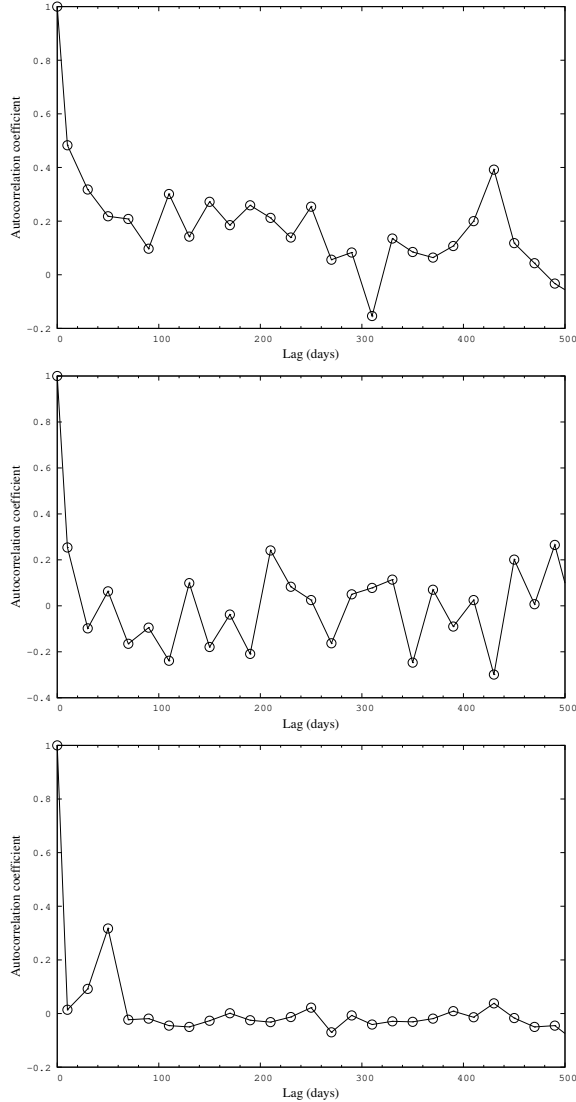


Figure 2. Autocorrelation analysis of the pulse detection rate variation shown in Figure 1, for PSR J1819–1458 (top panel), for PSR J1840–1419 (middle panel) and for PSR J1913–1330 (bottom panel).

detections was performed, eliminating pulses that are outside the expected pulse window, which are likely generated from sources of interference. This allowed us to study the burst rate and its evolution with time as detailed in §3.1. Then the barycentric TOAs for each single pulse are calculated by correlating it with a template of a strong pulse of the RRAT. As individual pulses are typically narrower, relatively broader templates based on the average profiles will not be suitable for correlating with the single pulses. The TOAs are modeled using the standard pulsar timing software TEMPO³, following exactly the same method as for normal pulsars (Lorimer & Kramer 2004).

³ tempo.sourceforge.net

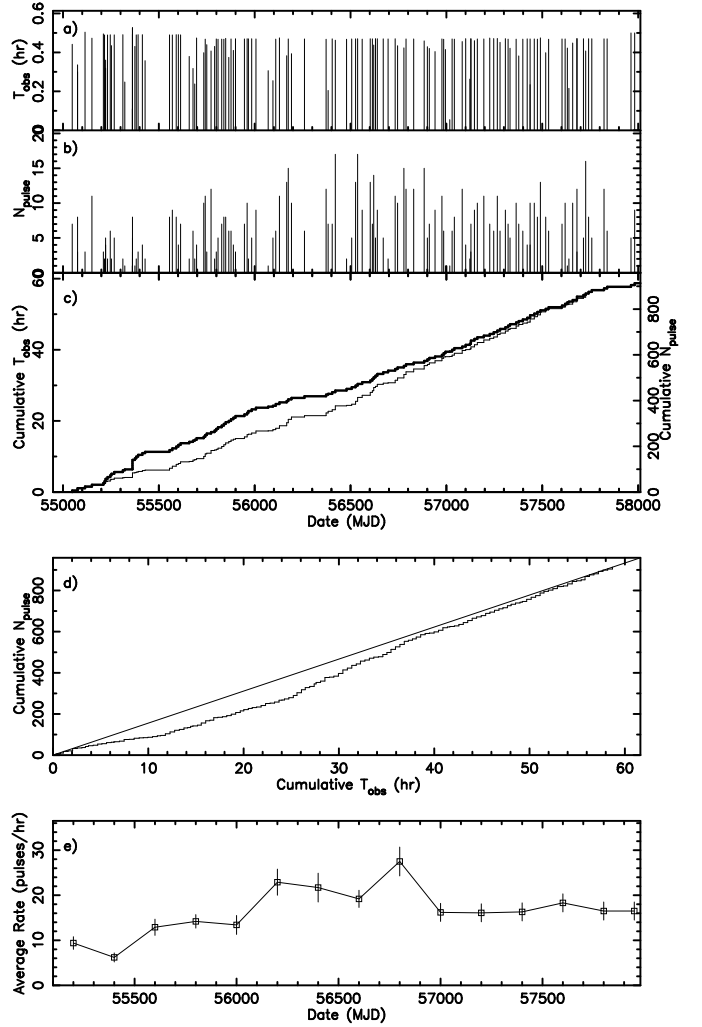


Figure 3. Statistics of pulses detected from PSR J1819–1458. (a) Duration of observation (T_{obs}) vs the epoch of observation (in MJD) in which the RRAT was detected, (b) Number of pulses (N_{pulse}) detected vs the epoch of observation (MJD), (c) Cumulative T_{obs} (with thin line) and Cumulative N_{pulse} (with heavy line) vs the epoch of observation, (d) Cumulative T_{obs} vs Cumulative N_{pulse} , solid line represents the mean burst rate over the range of observations shown, (e) Average rate (pulses/hr) vs the epoch (MJD).

3 RESULTS

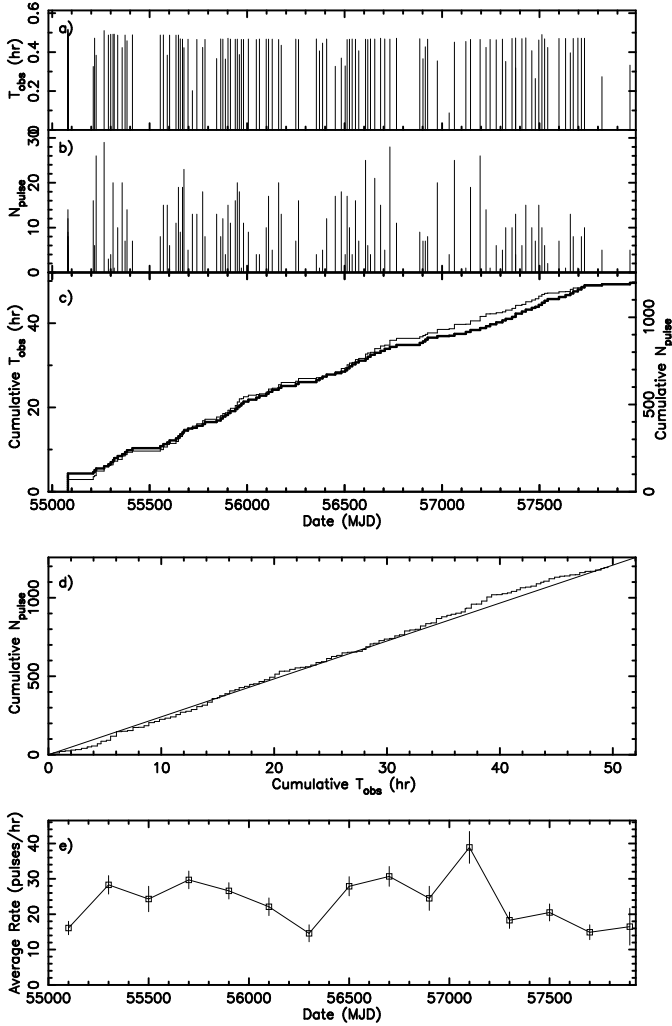
3.1 Pulse rate statistics

The RRATs were not detected in all observing epochs, in some cases because of RFI. PSR J1819–1458 was detected in 132 observing epochs out of 200 with a maximum detection rate of ~ 38 pulses/hour. PSR J1840–1419 was detected in 114 epochs out of 160 with a maximum detection rate of ~ 69 pulses/hour. PSR J1913+1330 was detected in 130 epochs out of 210 with a maximum detection rate of ~ 230 pulses/hour. We note that the duration of the observing epoch with detection rate of ~ 230 pulses/hour is relatively short (~ 6 mins) compared to the typical observing epochs (~ 30 mins). This indicates that emission rates from

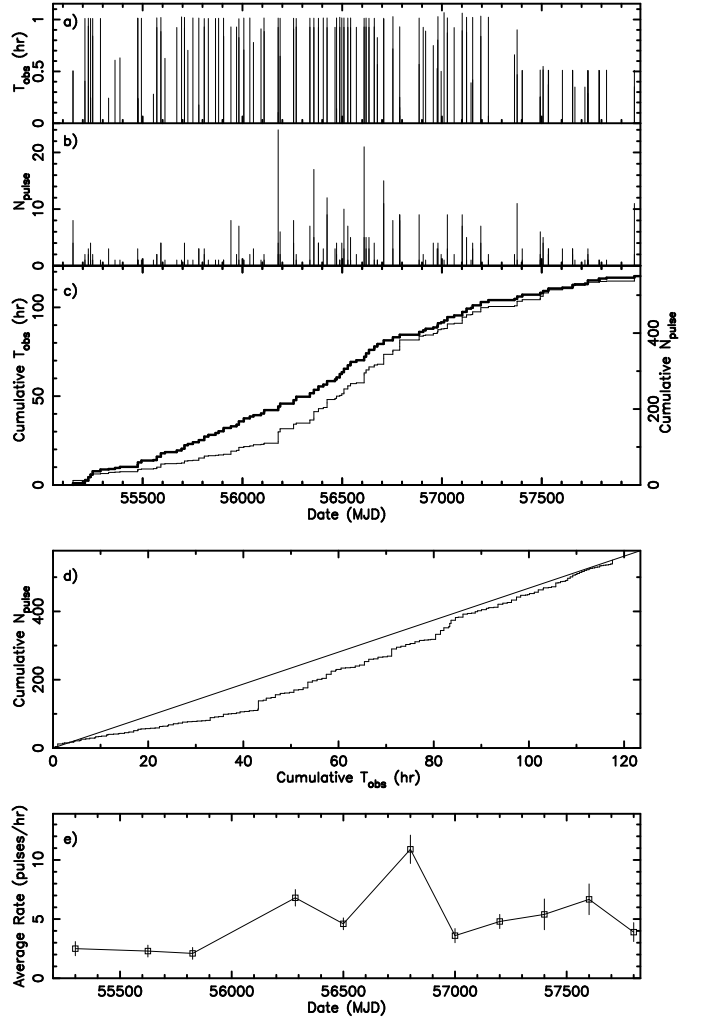
Table 1. Parameters for the straight line fitting, presented in Figure 1.

RRAT name	Slope	Intercept [†] (pulses/hr)	Reduced chi-square
J1819–1458	0.004±0.001	15.9±0.7	70
J1840–1419	−0.002±0.002	24.5±1.7	279
J1913+1330	0.0013±0.0005	4.9±0.5	32

[†] Epoch for the intercept is at MJD 56500

**Figure 4.** Statistics of pulses detected from PSR J1840–1419. The panels are as described for Figure 3.

RRATs can apparently reach a high value for short periods of time. Figure 1 shows the variation of the rate of pulse detection per hour for PSR J1819–1458, PSR J1840–1419 and PSR J1913+1330 based on the observations with the Lovell telescope. The rate of detection of the pulses varies greatly for all the three RRATs. We have fitted a linear relation to the detection rate versus date (MJD) data of these three RRATs. The slope and intercept of best fit straight lines for RRATs J1819–1458, J1840–1419 and J1913+1330

**Figure 5.** Statistics of pulses detected from PSR J1913+1330. The panels are as described for Figure 3.

are presented in Table 1. The reduced chi-square value for each fit is very high ($\gg 1$), indicating highly variable detection rates from day to day. The fitting indicate that there is a possibility of long-term increase in the detection rate for PSR J1819–1458. For PSR J1913+1330 there is marginal evidence of long-term increase in the detection rate; whereas no long-term change in the emission rate is observed for PSR J1840–1419.

For PSR J1819–1458 we observe an instance of apparently correlated change in emission rate, as seen from

MJD 55790 to MJD 55900 (data points joined by a solid line in top panel of Figure 1). There is some evidence of other periods where such features may have occurred but the cadence does not completely sample them. To investigate these possible correlations between pulse emission rates in nearby epochs, we conducted an autocorrelation analysis of the time sequence of Figure 1. The autocorrelations for RRATs J1819–1458, J1840–1419 and J1913+1330 calculated for lags up to 500 days with 20 days of resolution are presented in Figures 2. For PSR J1819–1458 there is some correlation for lags up to about 50 days. This is consistent with the structures seen in Figure 1(a). For PSR J1840–1458 and PSR J1913+1330 the autocorrelation function falls rather fast with increasing lag values. However, for PSR J1913+1330 a significant secondary peak is observed at a lag of 50 days.

To further investigate the pulse rate statistics we have plotted the cumulative duration of observation against the epoch of observation as was performed for two intermittent pulsars by Lyne et al. (2016). Figures 3, 4 and 5 present the pulse rate statistics for RRATs J1819–1458, J1840–1419 and J1913+1330 respectively. In these diagrams, panel (a) shows the duration of observation (T_{obs}) vs the epoch of observation (in MJD). The number of detected pulses (N_{pulse}) vs the epoch of observation (MJD) is plotted in panel (b). Panel (c) shows the cumulative T_{obs} (with thin line) and the cumulative N_{pulse} (with heavy line) versus the epoch of observation, whereas the cumulative T_{obs} versus the cumulative N_{pulse} is plotted in panel (d). In this diagram, the slope represents the local values of detected pulse rate. This can also be seen in panel (c) of Figures 3, 4 and 5, in which we observe that the cumulative T_{obs} and the cumulative N_{pulse} does not always have same slope. The rate of pulses vary significantly between epochs. This is in agreement with the inference from Figure 1. Table A1 lists the average pulse rates for the three RRATs for the full time span of observations and for smaller time spans, showing the evolution of average pulse rate with time. The average rate of pulses/hour (from Table A1) are plotted in panel (e) of Figures 3, 4 and 5. The average rates are similar to the fitted detection rate from Table 1 as expected. These also indicate a marginal increase in the detection rate observed for PSR J1819–1458 and PSR J1913+1330, and roughly constant detection rates for PSR J1840–1419.

3.2 Timing of J1819–1458

Figure 6 presents the timing residuals for all the pulses (above 5σ detection limit) from PSR J1819–1458 from September 2006 till August 2017, i.e. for ~ 11 years.

We observe that the pulsed-emission from PSR J1819–1458 is grouped within three separated longitude regions covering about 120 ms of pulse phase, which is also clearly seen in a histogram of the residuals (bottom left panel of Figure 6). The central band consists of $53\pm 2\%$ of the detected pulses whereas the early and late bands consist of $26\pm 1\%$ and $21\pm 1\%$ of pulses respectively. The three band structure is consistent with the observations from Lyne et al. (2009). To uniquely identify the three bands, we have considered data in three phase regions and separately fitted a model to identify the time offsets of three bands. To determine the band offsets, we put JUMP commands around

TOAs in early and late bands, and fitted using tempo with few spin-frequency derivatives as required to whiten the timing data. This resulted in offsets of -43.2 ± 1.5 ms between the central and the early band and $+46.1\pm 1.4$ ms between the central and late band respectively. The measured offsets are consistent with the ± 45 ms offset used in Lyne et al. (2009). The right panel of Figure 6 shows the residuals with the three bands aligned with these offsets. The rms of the residuals decreases from 31.4 ms for banded TOAs to 8.9 ms for the unbanded aligned TOAs. As a result of this procedure, the residuals are improved by a factor of 3.5 and uncertainties in the fitted parameters are similarly reduced.

Figure 7 shows the TOAs of PSR J1819–1458 from GBT observations at 2.2 GHz on 1st April 2008, with an rms of the residuals of 40 ms. The separation between the two outer bands is 98 ± 4 ms, which is $9\pm 1\%$ more than the 1.4 GHz separation. This is indicative of a wider emission region at 2.2 GHz than 1.4 GHz, which is in the opposite direction to that predicted by radius to frequency mapping (Cordes 1978). In addition we observe that at 2.2 GHz, unlike 1.4 GHz, the majority of the pulses are not from the central band and the central band TOAs are frequently split in two bands. Figure 8 shows examples of single pulses from PSR J1819–1458, with a few having complex profiles including single, double and triple peaks.

3.2.1 Post-glitch frequency evolution

Glitches are sudden jumps of rotational period and are detected as a result of regular monitoring of a pulsar. A timing model fitting ν , $\dot{\nu}$, $\ddot{\nu}$ to the pre-glitch TOAs usually describes the pulsar rotation, but after a glitch one needs to have a new timing model for fitting the post-glitch TOAs. In the timing campaign described in Lyne et al. (2009), they detected two glitches at MJD ~ 53924 and ~ 54168 , and studied the post-glitch timing properties for ~ 800 days after the glitches. In the present work, we find no further glitches, but carry out further investigation of the post-glitch rotational properties of PSR J1819–1458 for about 3700 days. Table 2 presents the pre-glitch and post-glitch timing models for PSR J1819–1458. Figure 9 shows the frequency evolution of PSR J1819–1458 over about 18 years. Panel (a) shows the slow down of the RRAT and the large glitch observed at MJD ~ 53924 . We fit a simple slow down model (fitting only pulsar frequency and its derivative) to the data between MJD 51000 and 53900 and a second relatively smaller glitch is now visible in panel (b) at MJD ~ 54168 . The post-glitch time evolution of the frequency derivative $\dot{\nu}$ plotted in panel (c), can be classified in a few stages:

- (i) Rapid increase of $|\dot{\nu}|$: a rapid increase of $|\dot{\nu}|$ is observed immediately after the glitch, $|\dot{\nu}|$ is $\sim 31.6 \times 10^{-15}$ Hz s^{-1} before the glitch and immediately after the glitch $\dot{\nu}$ increases to $\sim 35.0 \times 10^{-15}$ Hz s^{-1} .
- (ii) Post-glitch recovery of $|\dot{\nu}|$: Next $|\dot{\nu}|$ exponentially decreases.
- (iii) Over-recovery of the $|\dot{\nu}|$: $|\dot{\nu}|$ reaches an asymptotic value of $\sim 31.0 \times 10^{-15}$ Hz s^{-1} , which is significantly smaller than the pre-glitch value of $\sim 31.6 \times 10^{-15}$ Hz s^{-1} .
- (iv) Recovery from over-recovery of $|\dot{\nu}|$: After MJD ~ 55000 , the $|\dot{\nu}|$ again starts to increase and reaches $\sim 31.1 \times 10^{-15}$ Hz s^{-1} at the time of writing this paper.

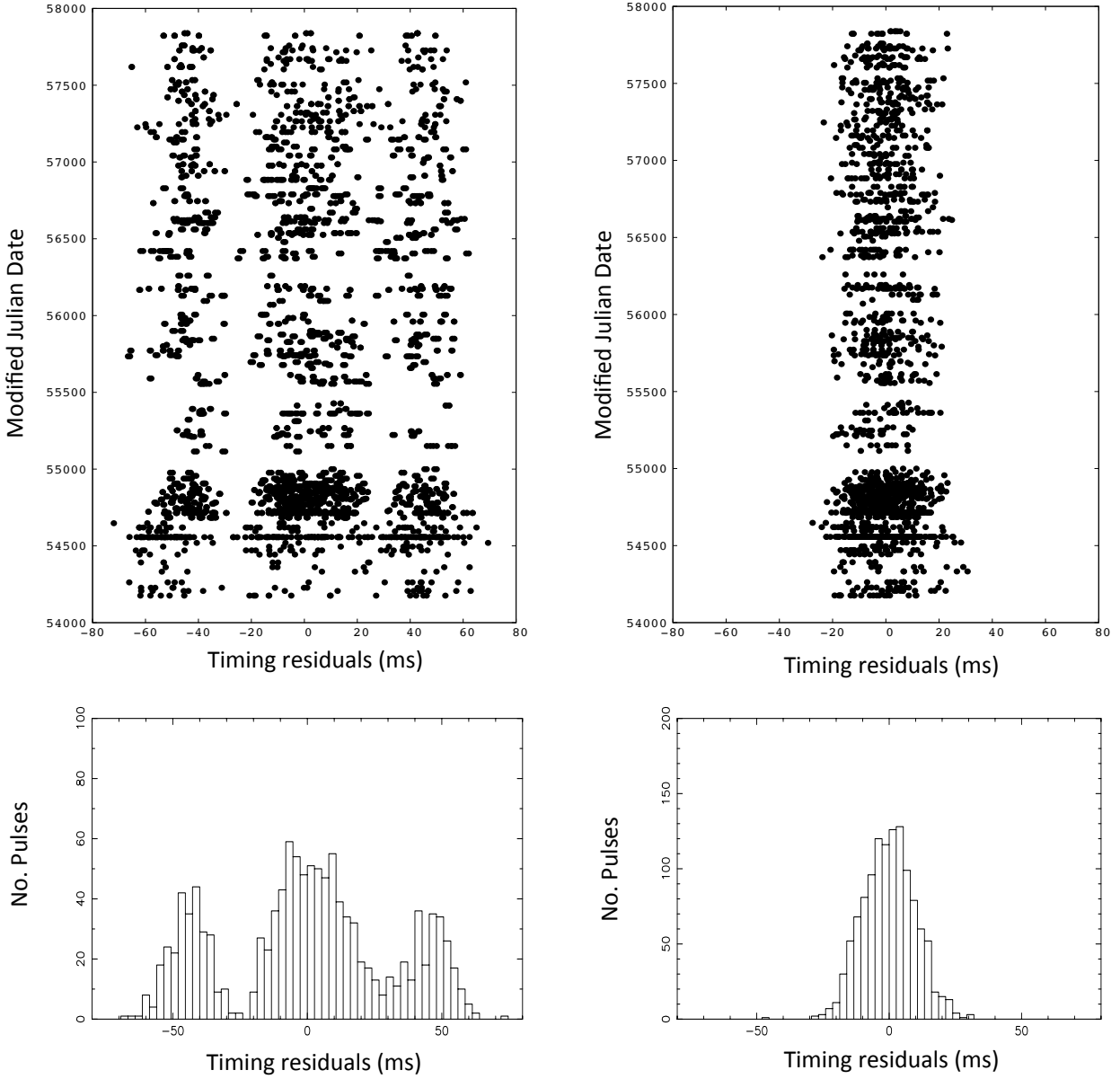


Figure 6. Left panel: The timing residuals from the TOAs from the Lovell and the Parkes observations at L-band of the individual pulses from PSR J1819–1458 from post-glitch observations (relative to the model in Table 2) for ~ 3900 days i.e. ~ 11 years, showing that the majority of TOAs are located in three clearly identifiable bands with the accumulated arrival time histograms shown below. Right panel: The same residuals, but with the TOAs in the early and late bands fitted using offsets of -43.2 ± 1.5 ms and $+46.1 \pm 1.4$ ms relative to the central band, to produce unbanded residuals, with the accumulated arrival time histogram shown below. The rms of the residuals subsequently decreases from 31.4 to 8.9 ms.

Glitches observed in other pulsars are also characterised by stages like (i) and (ii). However, for PSR J1819–1458 we observe that the recovery of the frequency derivative goes beyond the pre-glitch value and we observe stages (iii) and (iv), which is not the case for the other pulsars (aside from PSR J1119–6127, [Weltevrede et al. \(2011\)](#)). The implication of this result and comparison with the post-glitch timing properties of normal pulsars are discussed further in §4.

3.3 Timing of PSR J1840–1419

The left panel of Figure 10 shows the timing residuals from TOAs of the individual pulses from PSR J1840–1419 over ~ 8 years relative to the slow down model in Table 3. This model obtained by fitting for ν , $\dot{\nu}$, $\ddot{\nu}$ and pulsar position results in timing residuals with an rms of 12.6 ms. Although the observed spread in the residuals is $\sim \pm 40$ ms, the majority of TOAs are within $\sim \pm 20$ ms. The histogram of the timing residuals is shown in the bottom panel.

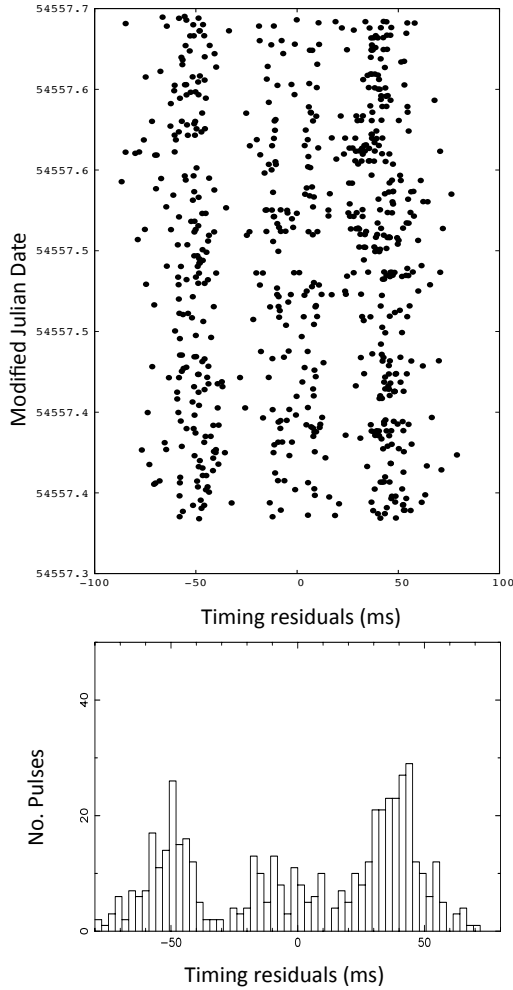


Figure 7. The timing residuals from the TOAs of the individual pulses from PSR J1819–1458, from the GBT observations at 2.2 GHz on 1st April 2008, (relative to the model in Table 2) showing that TOAs at this frequency are also distributed in bands (top panel). The rms residual is 40.6 ms. The histogram of the residuals is shown in the bottom panel.

3.4 Timing of PSR J1913+1330

The right panel of Figure 10 shows the timing residuals of PSR J1913+1330 over ~ 12 years, relative to a timing model given in Table 3 derived after fitting for ν and its first four derivatives and pulsar position, resulting in timing residuals with an rms of 1.0 ms. The histogram of the timing residuals is shown in the bottom panel. The right panel of Figure 11 presents the average profile of the RRAT pulses detected for J1913+1330 (created with the PSRSALSA software package Weltevrede et al. (2016)).

3.5 Weak emission mode for PSR J1913+1330

In addition to the RRAT pulses, we report the detection of a persistent but weak emission mode for PSR J1913+1330. The weak mode is observed after averaging pulses together and is followed by a long absence of any detectable emission. We marked time slices with a pulse detected at more

Table 2. Timing parameters of PSR J1819–1458

Pre-glitch parameters (Lyne et al. 2009)	
Right ascension (J2000)	18 ^h 19 ^m 34 ^s .173 [†]
Declination (J2000)	−14°58′03″.57 [†]
Pulsar frequency ν (s ^{−1})	0.23456756350(2)
Pulsar frequency derivative $\dot{\nu}$ (s ^{−2})	−31.647(2)×10 ^{−15}
Period epoch (MJD)	54451
Timing data span (MJD)	51031–54938
Dispersion measure DM (pc cm ^{−3})	196.5
Post-fit residual rms (ms)	10.2
Glitch 1 parameters	
Epoch (MJD)	53924.79(15)
Incremental $\Delta\nu$ (Hz)	0.1380(6)×10 ^{−15}
Glitch 2 parameters	
Epoch (MJD)	54168.6(8)
Incremental $\Delta\nu$ (Hz)	0.0226(3)×10 ^{−6}
Post-glitch parameters	
Right ascension (J2000)	18 ^h 19 ^m 34 ^s .16(1)
Declination (J2000)	−14°58′00″.00(1)
Pulsar frequency ν (s ^{−1})	0.234564843(4)
Pulsar frequency derivative $\dot{\nu}$ (s ^{−2})	−30.959(4)×10 ^{−15}
Pulsar frequency second derivative $\ddot{\nu}$ (s ^{−3})	−1.24(2)×10 ^{−24}
Pulsar frequency third derivative $\dddot{\nu}$ (s ^{−4})	−2.4(6)×10 ^{−33}
Pulsar frequency fourth derivative $\nu^{(4)}$ (s ^{−5})	−3.0(8)×10 ^{−39}
Pulsar frequency fifth derivative $\nu^{(5)}$ (s ^{−6})	−1.1(4)×10 ^{−47}
Period epoch (MJD)	55996.24
Timing data span (MJD)	54175.87–57838.37
Dispersion measure DM (pc cm ^{−3})	196.5
Number of TOAs	1373
Post-fit residual rms (ms)	8.9
Derived parameters	
Period (s)	4.2632901504(1)
Period Derivative	5.62717(4)×10 ^{−13}
Braking Index from $\nu, \dot{\nu}, \ddot{\nu}$	−226
Total time span (yr)	10.03
Spin down energy loss rate \dot{E} (erg/s)	2.8×10 ³²
Spin down age (yr)	1.2×10 ⁵
Surface magnetic flux density (Gauss)	4.9×10 ¹³
DM distance [‡] (kpc)	3.3

[†] errors are 2″ as derived from Chandra observations (Rea et al. 2009)

[‡] using Yao et al. (2017) model of electron distribution

than 5σ signal-to-noise in a 1 minute integration as a detection of the weak mode emission. The duration of the weak emission mode varied from 2 minutes to 14 minutes during our observations. Interestingly, strong RRAT pulses were not present during the weak mode intervals. The left panel of Figure 11 presents the average profile of the pulses detected in its weak mode. Though the average profile for the burst mode is single-peaked, we see a double peaked-profile for the weak emission mode. The mean flux density of the pulses in the weak emission mode is lower than the mean of the RRAT pulses by about a factor of 50. Figure 12 plots the emission statistics of this weak average emission mode which can be compared to the emission statistics of bright single pulses typically seen for the RRATs (Figure 5). Table A1 compares the rate of emission (in pulses/hr) for the

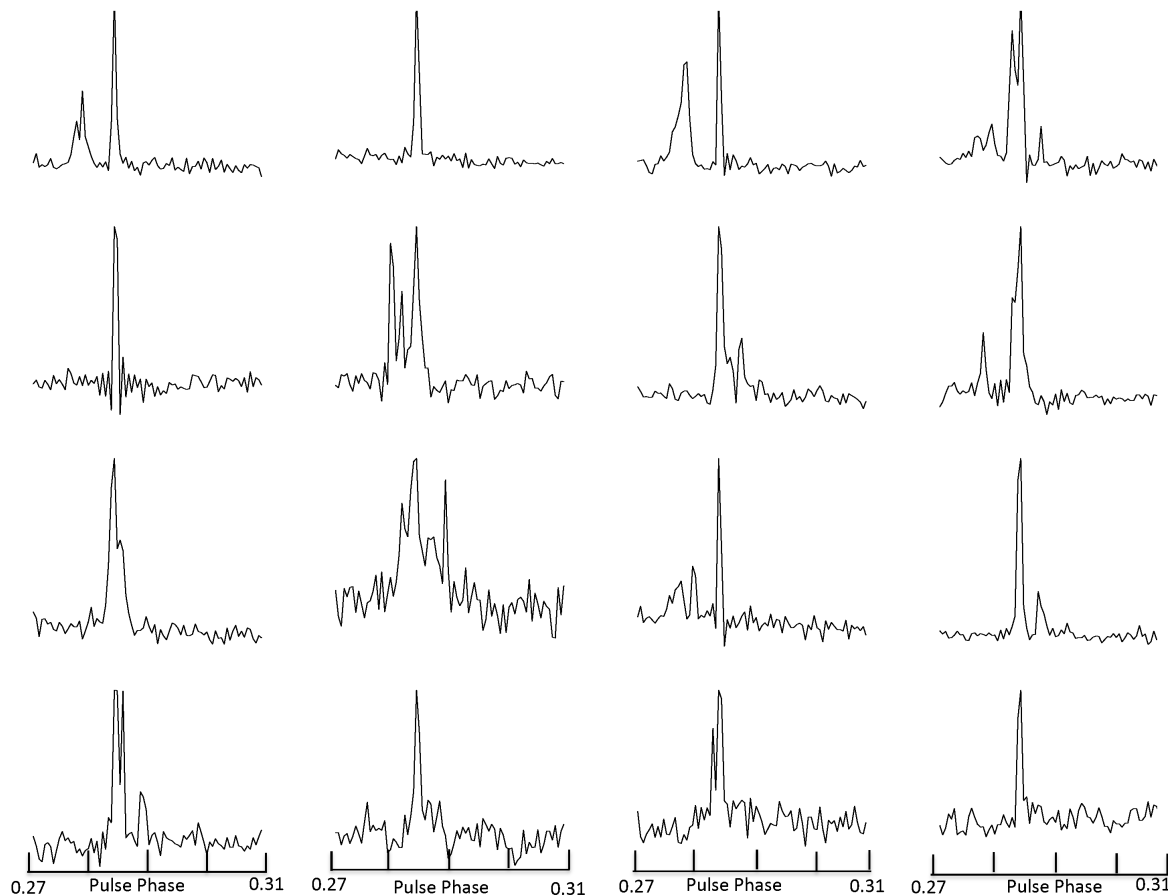


Figure 8. A selection of single pulses detected from PSR J1819–1458, showing that individual pulses vary greatly and have complex profile structures.

RRAT mode and the weak emission mode. The average rate of pulse emission in the weak mode is ~ 64 pulses/hr, which is at least an order of magnitude higher than the rate of emission in RRAT mode. This assumes that all pulses accumulated in the weak mode have similar strengths. With this assumption, the total detection of pulses in the weak mode translates to ~ 7000 pulses in ~ 110 hours of observation. This indicates that the weak mode emission is detected for 1.6% of the total observing duration. We note that PSR J1913+1330 emits bright single pulses typical for RRATs for 0.1% of the total observing duration.

4 DISCUSSION AND SUMMARY

We now discuss the main outcomes and the corresponding implications of this work.

4.1 Pulse rate statistics

We have studied pulse rate statistics using the data from the Lovell telescope for three RRATs. We report a possible long-term increase in the emission rate for PSR J1819–1458 (Figure 1). We also see evidence for a marginal increase in pulse emission rate for J1913+1330, but for PSR J1840–1419

no long-term change in emission rate is observed. For PSR J1840–1419, Keane et al. (2011) determined a RRAT pulse emission rate of ~ 60 pulse/hour for a study during MJD 54909–55239 using the Parkes telescope, which is considerably higher than the average of ~ 25 pulse/hour from our study with the Lovell telescope possibly due to the use of a smaller bandwidth and a worse RFI environment. For PSR J1913+1330, McLaughlin et al. (2009) determined a rate of ~ 1.5 pulses/hour during MJD 53035–54938 with the Lovell telescope. This differs by at least a factor of two from the average detection rate of ~ 4.9 pulses/hour for the duration of MJD 55150–57400 listed in Table A1. This may be due to use of the more sensitive DFB backend during our study compared to the narrower band AFB, or may indicate a long-term increase in the pulse rate.

We report significant variations of the pulse rates between the observing epochs. We reported emission rates of ~ 230 pulses/hour and ~ 123 pulses/hour for two observing epochs for PSR J1913+1330. However, since both these epochs are relatively short (~ 6 mins) compared to the typical 30 mins observing epochs, it is likely that we managed to hit on a period of time when the RRAT was active. Variations of two orders of magnitude from the mean pulse rates at individual epochs has implications for possible RRAT emission models. Giant pulses from weak pulsars is one of the possible explanations for RRAT emission. Lundgren et al. (1995)

Table 3. Timing parameters of PSR J1840–1419 and J1913+1330

Parameters	J1840–1419	J1913+1330
Right ascension (J2000)	18 ^h 40 ^m 33 ^s .04(1)	19 ^h 13 ^m 17 ^s .97(1)
Declination (J2000)	−14°19′06″.5(9)	−13°30′32″.78(4)
Pulsar frequency ν (s ^{−1})	0.151571128974(2)	1.0829644010729(3)
Pulsar frequency derivative $\dot{\nu}$ (s ^{−2})	−1.4597(3)×10 ^{−16}	−1.01772(2)×10 ^{−14}
Pulsar frequency double derivative $\ddot{\nu}$ (s ^{−3})	−1.6(1.4)×10 ^{−27}	6(5)×10 ^{−27}
Pulsar frequency triple derivative $\dddot{\nu}$ (s ^{−4})	–	−6.9(3)×10 ^{−33}
Pulsar frequency fourth derivative $\nu^{(4)}$ (s ^{−5})	–	7(1)×10 ^{−41}
Period epoch (MJD)	55074.9	55090.9
Timing data span (MJD)	54909.889–57820.378	53491.80–57964.82
Dispersion measure DM (pc cm ^{−3})	20.0	175.6
Number of TOAs	1438	815
<hr/>		
Post-fit residual rms (ms)	12.6	1.1
<hr/>		
Derived parameters		
<hr/>		
Period (s)	6.5975625223(1)	0.923391386650(2)
Period Derivative	6.353(1)×10 ^{−15}	8.6776(2)×10 ^{−15}
Braking Index from $\nu, \dot{\nu}, \ddot{\nu}$	−11986	63.54
Total time span (yr)	7.97	12.46
Spin down energy loss rate \dot{E} (erg/s)	8.7×10 ²⁹	4.2×10 ³²
Spin down age (yr)	1.6×10 ⁷	1.6×10 ⁶
Surface magnetic flux density (Gauss)	6.5×10 ¹³	2.8×10 ¹²
DM distance [†] (kpc)	0.73	6.1

[†] using Yao et al. (2017) model of electron distribution.

reported that though the observed rate of giant pulse emission from the Crab pulsar changes from day to day, above a fixed threshold the rate of all the giant pulses emitted remains fixed and observed variability is caused by propagation effects in the interstellar medium. Therefore, whether the observed two orders of magnitude variation in pulse detection rate for PSR J1913+1330 can be explained by propagation effects may influence the feasibility of giant pulse like origin of the RRAT pulses. The other proposition of for RRAT behaviour being extreme nulling of radio pulsars a with randomly varying active and null state is still a feasible mechanism. Circumstellar asteroid belts around the pulsar (Cordes et al. 2008) could be feasible subject to the requirement to explain such highly varying emission rates.

4.2 Long-term timing of RRATs

We present long-term radio timing results for RRATs J1819–1458, J1840–1419 and J1913+1330. For timing of most pulsars we use integrated profiles, which are stable and phase stability is implicitly assumed. However, for single pulse timing this assumption is not valid and extra scatter in the timing residuals is expected and is clearly seen in Figure 6 and 10. For PSR J1819–1458 we have seen that the shape of the individual pulses varies greatly, which is also commonly seen for normal pulsars. However, the distribution of pulse arrival times from PSR J1819–1458 at 1.4 and 2.2 GHz indicate a trend opposite to the radius to frequency mapping generally followed by pulsars. It will be intriguing to study the frequency-evolution of the separation of profile components over a wider frequency and with simultaneous data.

This is the longest time-span study performed for RRATs so far and therefore enables us to compare the long-

term timing properties of the RRATs with the other pulsars. Figure A1 shows the RRATs studied in this paper in the $P - \dot{P}$ diagram along with other pulsars and RRATs. We find that the long-term timing properties of these RRATs are similar to the other pulsars. We note that the estimated surface magnetic field strength of J1819–1458 is the highest known among RRATs.

For the pulsars that emit giant pulses, the inferred magnetic field strength at the light cylinder $B_{LC} \propto P^{2.5} \dot{P}^{0.5}$ is an indicator of giant pulse emissivity (e.g Knight et al. (2006), Cognard et al. (2004)), with $B_{LC} > 10^5$ G for the giant pulse emitting pulsars. However, Knight et al. (2006) argue that $\dot{E} \propto P^{-3} \dot{P}$ rather than B_{LC} may be a better indicator of giant pulse emission. B_{LC} and \dot{E} of the three RRATs studied in this paper (inferred from Tables 2 and 3) are many order of magnitude less than the proposed values. Moreover, as the pulses detected from RRATs are much broader (\sim milliseconds) than the traditional giant pulses (\sim nano-seconds), this argues against RRAT pulses being a manifestation of giant pulse emission.

4.3 Post-glitch timing properties of PSR J1819–1458

We studied the timing properties of J1819–1458 for over 6500 days, and report unique post-glitch timing properties for about 3700 days after the glitch at MJD 54167. A long-term decrease of $|\dot{\nu}|$ following the glitch is observed, implying that the pulsar position in the $P - \dot{P}$ diagram shifts vertically downwards after the glitches as reported by Lyne et al. (2009). Glitches observed for other pulsars result in an abrupt increase of $|\dot{\nu}|$ during the glitch, which then decreases after the glitch and stabilises resulting in a long-term

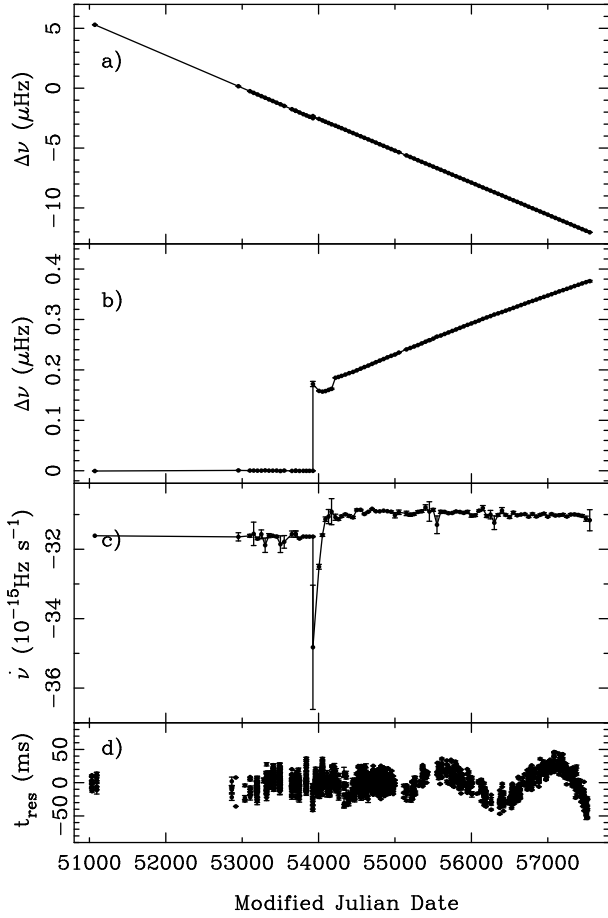


Figure 9. Rotational evolution of PSR J1819–1458 over about an 18-year duration: (a) the spin-down in rotation rate of the RRAT, interrupted by a major glitch at MJD ~ 53924 , (b) the frequency residuals relative to a simple spin-down model fitted to data between 51000 and 53900, showing the second, relatively smaller, glitch at MJD ~ 54168 , (c) the frequency derivative $\dot{\nu}$, showing the rapid increase in the magnitude of the spin-down rate immediately after the glitch, followed by a quasi-exponential decay and ultimately a gradual and slow increase of the slow down rate. (d) the timing residuals relative to the rotational model given in Table 2. The noisier residuals near the end of the data set are possibly due to a change in $|\dot{\nu}|$.

increase in spin-down rate. For example, Espinoza et al. (2011) presented a database of 315 glitches from 102 pulsars and showed that the result of a frequency-glitch in normal pulsars is a net increase in slow down rate (Figure 6 of Espinoza et al. (2011)) and an upwards step in the $P-\dot{P}$ diagram. Repeated occurrence of such glitches involving a long-term decrease of $|\dot{\nu}|$, in J1819–1458, would imply that this RRAT will gradually move from magnetar-like spin properties to those of radio pulsars. Since it is difficult to explain the observed post-glitch evolution of $\dot{\nu}$ with the conventional model of sudden unpinning of the vortex lines and subsequent transfer of angular momentum from the super-fluid

to the crust, Lyne et al. (2009) pointed out that observed glitches in PSR J1819–1458 could be magnetar like. Such glitches are frequently observed for the magnetars, and are thought to originate due to the high internal magnetic field that can deform or crack the crust (Thompson et al. 1996).

PSR J1119–6127 is another radio pulsar to show a similar post-glitch long-term decrease of $|\dot{\nu}|$ (Weltevrede et al. 2011). Incidentally PSR J1119–6127 also has a high surface magnetic field ($B \sim 4.1 \times 10^{13}$ G), like PSR J1819–1458 ($B \sim 4.94 \times 10^{13}$ G). Antonopoulou et al. (2014) termed such a peculiar post-glitch behaviour as “over-recovery” of the spin-down rate and suggested that they were magnetar-like glitches. Recently, Archibald et al. (2016) have reported a magnetar like outburst from this pulsar. Similar “over-recovery” in frequency is also reported for a X-ray pulsar J1846–0258 (Livingstone 2010). It also has a relatively high inferred magnetic field ($B \sim 5 \times 10^{13}$ G). Such interesting magnetar like properties of high magnetic field pulsars, and similarity in glitch properties with PSR J1119–6127, emphasise the importance of regular monitoring of PSR J1819–1458.

After the episode of “over-recovery” immediately after the glitch for PSR J1819–1458, we observe a very slow “recovery from the over-recovery” (i.e. $|\dot{\nu}|$ again starts to increase consistently) starting significantly later (~ 1000 days after the glitch episode) and continuing until the point of writing this paper. It is possible that eventually the pre-glitch $\dot{\nu}$ value will be reached with such a recovery process if it is not interrupted by another glitch. Lyne et al. (2009) commented that for PSR J1819–1458 the spin-down rate will decay to zero on a time scale of few thousand years if the pulsar underwent similar glitches every 30 years resulting in a permanent decrease in slow-down rate (i.e. a step down in the $P-\dot{P}$ diagram). However, the “recovery from the over-recovery” observed by us for this pulsar will play a major role in deciding how the slow down rate will evolve and the predicted time for the spin-down rate to reach to zero, if at all. It is also possible that before the next glitch the “recovery from the over-recovery” places the RRAT at its original position of the $P-\dot{P}$ diagram. We note that even ~ 3700 days after the glitch, the effects of the glitch persist, indicating a very long-term memory of the process. Theoretical models explaining the glitch phenomena will be constrained by this and it will be interesting to see if the occurrence of the next glitch is random or has some relation with the recovery process. Moreover, since PSR J1819–1458 is the only RRAT for which glitches are observed, it will be interesting to know if these glitches are representative of RRATs. This can only be verified with regular monitoring to detect possible glitches in other RRATs.

4.4 Weak emission mode for PSR J1913+1330

In addition to regular active and off modes observed for RRATs, we have detected a second weak emission mode for PSR J1913+1330 (detailed in §3.5), characterised by weak average emission followed by long absence of detectable emission. This is reminiscent of profile mode changing and nulling which are commonly observed for many pulsars. But PSR J1913+1330 is the only RRAT for which such weak emission is observed besides the normal active and off modes for RRATs. We also observe a difference in profile shape in the two modes. For the RRAT mode the average profile

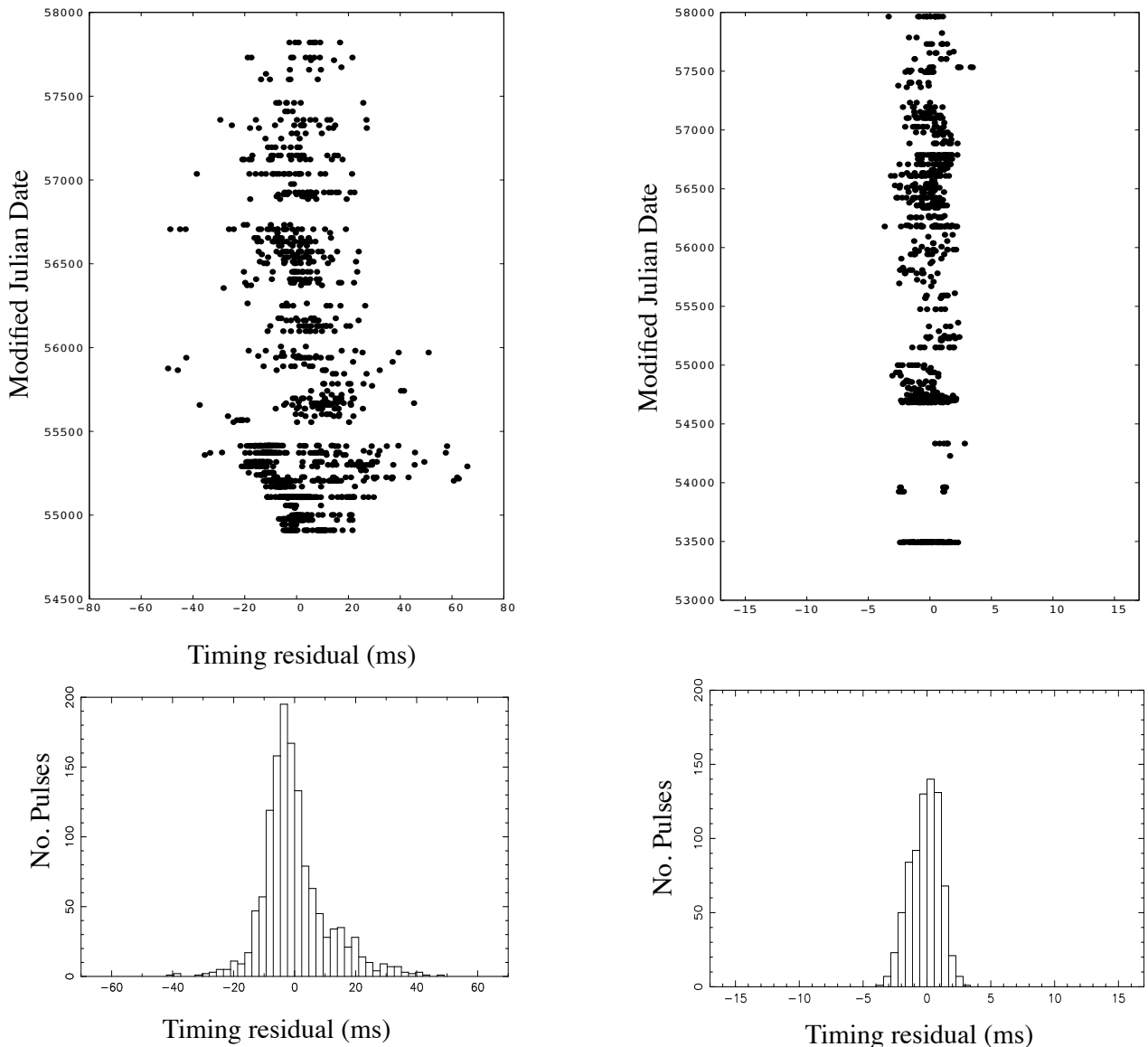


Figure 10. Left panel: The timing residuals from the TOAs of the individual pulses from PSR J1840–1419 for ~ 2900 days i.e. ~ 8 years, relative to the timing model given in Table 3, fitting for pulsar frequency ν , its first two derivatives and pulsar position, resulting in residuals with an rms value of 12.6 ms. The histogram of the corresponding timing residuals is shown in the bottom panel. Right panel: The timing residuals from the TOAs of the individual pulses from PSR J1913+1330 for ~ 4480 days i.e. ~ 12 years, relative to a slow down model given in Table 3, fitting pulsar frequency ν , its first five frequency derivatives and pulsar position, giving an rms of 1 ms. The histogram of the corresponding timing residuals is shown in the bottom panel.

is single-peaked, whereas for the weak mode the profile is double-peaked. We find that the mean flux density of the RRAT pulses is ~ 50 times higher than that of typical pulses in the weak emission mode. We also report that the total duration of the weak mode emission is at least an order magnitude higher than the total duration of RRAT single pulses. Finding a different mode of emission, similar to emission from normal pulsars, in RRATs has implications in understanding the connection between their emission processes. This indicates that the RRATs may be a manifestation of extreme nulling pulsars, in this case also with a very weak emission mode.

The long-term study by Young et al. (2015) found that

PSR J1853+0505 exhibits a weak emission state, in addition to its strong and null states. This indicates that nulls may represent transitions to weaker emission states which are below the sensitivity thresholds of particular observing systems. However, for most pulsars nulling is observed to be followed by emission for more than one pulse period. This is in contrary to the fact that most observed RRAT pulses are single. So RRATs could be a special manifestation of nulling that is not generally observed for normal pulsars.

In a study of PSR B0656+14, which was argued to have similar emission properties as RRATs if it is placed at a large distance, Weltevrede et al. (2006), had postulated that longer observations of RRATs may reveal weaker emission

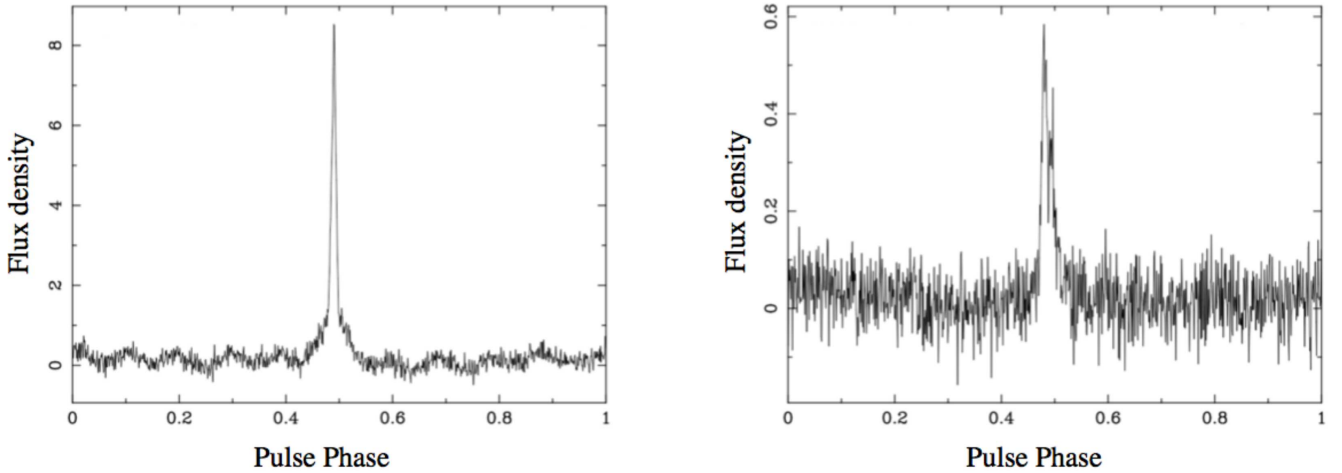


Figure 11. Left panel: Average profile of the RRAT pulses detected for PSR J1913+1330 (~ 540 pulses). Right panel: Average profile of the weak mode detected for the PSR J1913+1330 (~ 7000 pulses). Flux density is in arbitrary units, but the two plots are on the same scale.

modes in addition to the detected RRAT pulses. Detection of a weak emission mode for PSR J1913+1330 may strengthen this hypothesis. However, it is noteworthy that, although the RRAT population have typically larger period and magnetic field strengths than the normal radio pulsar population (Figure A1), the spin-down properties of PSR J1913+1330 are similar to those of the normal radio pulsar population. Thus PSR J1913+1330 is a special RRAT sharing properties of both the populations. Another similar pulsar is PSR J0941–39 which exhibits an RRAT-like emission rate of $\sim 90/100$ pulses/hour at times and behaves like a strong pulsar with nulling at other times (Burke-Spolaor et al. 2010). Searching for such weak emission modes in other RRATs will be important in this context.

To conclude, we present the longest time span study of three RRATs. In addition, we described the detection-rate evolution, unusual post-glitch properties of PSR J1819–1458 and detected a pulsar-like emission mode for PSR J1913+1330. Instead of being a separate class of neutron star, RRATs can be manifestations of extreme emission types that are previously not seen in the rest of the neutron star population. Unraveling this will require comparison of timing properties of a large number of RRATs. But a large fraction of RRATs are not well studied, for example about 70% of the known RRATs do not have a timing solution. Detailed long-term study of RRATs is warranted to establish the connection of RRATs with the rest of the neutron star population.

5 ACKNOWLEDGMENTS

We thank reviewer of this paper for comments that helped us to improve the paper. B. Bhattacharyya acknowledges support of Marie Curie grant PIIF-GA-2013-626533 of European Union. Pulsar research at Jodrell Bank centre for Astrophysics and access to the Lovell telescope is supported by a Consolidated Grant from the UK’s Science and Technology Facilities Council. The Parkes radio telescope is part of the Australia Telescope National Facility which is funded by the Australian Government for operation as a National Facility managed by CSIRO. The Green Bank Observatory is a facility of the National Science Foundation operated

under cooperative agreement by Associated Universities, Inc. We thank A. Holloway and R. Dickson of University of Manchester for making the Hydrus computing cluster at University of Manchester available for the analysis presented in this paper.

REFERENCES

- Antonopoulou D., Weltevredre P., Espinoza C. M., Watts A. L., et al. 2015, *ApJ*, 447, 2047.
- Archibald R. F., Kaspi V. M., Tendulkar S. P., & Scholz P. 2016, *ApJL*, 829, 1.
- Burke-Spolaor S., Bailes M., 2010, *MNRAS*, 402, 855.
- Camero-Arranz A., Rea N., Bucciantini, N et al., 2013, *MNRAS*, 429, 2493.
- Cordes J. M., Shannon R. M., 2008, *ApJ*, 682, 1152.
- Cordes J. M., 1978, *ApJ*, 222, 1006.
- Cognard, I. & Backer, D. C. 2004, *ApJ*, 612, L125.
- Cui, B. Y., Boyles, J., McLaughlin, M. A., Palliyaguru, N., 2017, *ApJ*, 840, 5.
- Dhillion V. S., Keane, E. F., Marsh, T. R. et al. 2011, 414, 3627.
- Eatough R. P., Keane E. F., Lyne A. G., 2009, *MNRAS*, 395, 410.
- Espinoza C. M., Lyne A. G., Stappers B. W., 2011, *MNRAS*, 414, 1679.
- Gehrels N., 1986, *ApJ*, 303, 336.
- Hankins, T. H., Kern, J. S., Weatherall, J. C., & Eilek, J. A. 2003, *Nature*, 422, 141.
- Hobbs et al. 2004, 353, 1311.
- Keane E. F., Ludovici D. A., Eatough R. P. et al. 2010, *MNRAS*, 401, 1057.
- Keane E. F., Kramer M., Lyne A. G. et al. 2011, *MNRAS*, 415, 3065.
- Keane E. F., McLaughlin, M. A.; Kramer, M.; Stappers, B. W. et al. 2013, *ApJ*, 764, 180.
- Knight H. S., Bailes M., Manchester R. N., Ord S. M., Jacoby B. A., 2006, *ApJ*, 640, 941.
- Karastergiou A., Hotan A. W., van Straten W., McLaughlin M. A., Ord S. M., 2009, *MNRAS*, 396, L95.
- Lorimer, D. R., & Kramer, M., 2004, *Handbook of Pulsar Astronomy*, Vol. 4. Cambridge, UK, 211.
- Livingstone, M. A., Kaspi V. M., Gavriil F. P. 2010, *ApJ*, 710, 1710.
- Lundgren S. C., Cordes J. M., Ulmer M. et al., 1995, *APJ*, 453, 433.

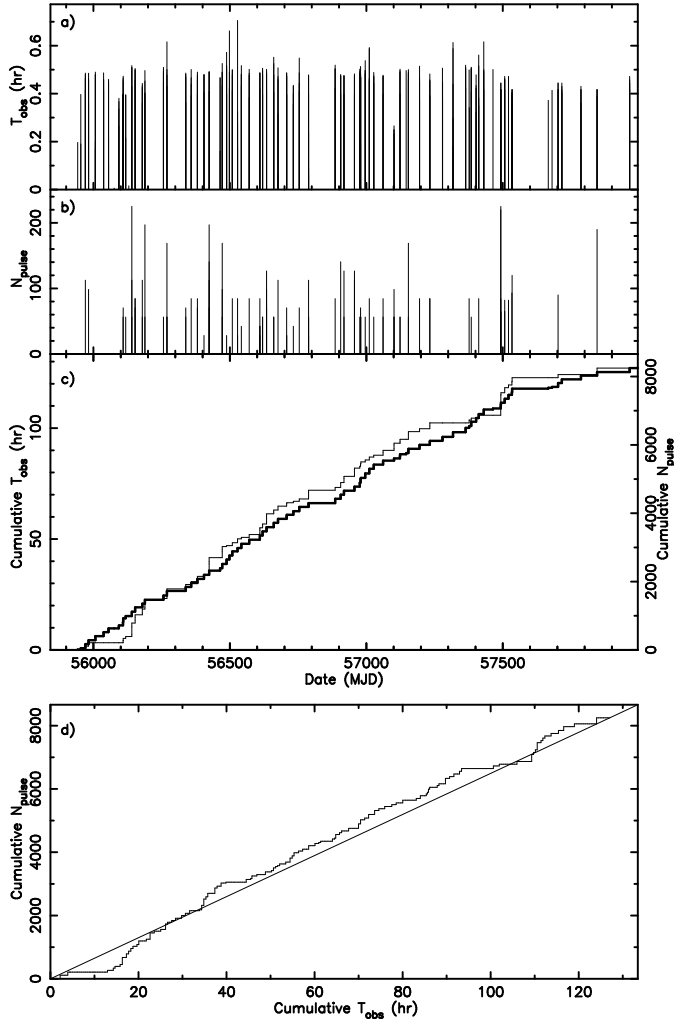


Figure 12. Average emission statistics of PSR J1913+1330 for the weak mode. (a) Duration of observation (T_{obs}) vs the epoch of observation (in MJD) in which average emission from the RRAT was observed, (b) Number of pulses (N_{pulse}) equivalent of average emission detected vs the epoch of observation (MJD), (c) Cumulative T_{obs} (with heavy line) and Cumulative N_{pulse} (with thin line) vs the epoch of observation, (d) Cumulative T_{obs} vs Cumulative N_{pulse} ; solid line represents the mean emission rate considering the start and stop range of observations.

- Lyne, A. G., Stappers, B. W., Freire, P. C. C. et al. 2016 (submitted to ApJ).
 Lyne, A. G., McLaughlin, M. A., Keane, E. F. et al. 2009, MNRAS 400, 1439.
 Manchester, R. N., Hobbs, G. B., Teoh, A. & Hobbs, M. 2005, AJ, 129.
 McKee, J. Janssen, G. H., Stappers, B. W. et al. 2016, MNRAS, 461, 2809.
 McLaughlin, M. Lyne, A. G., Lorimer, D. R. et al. 2006, Nature, 439, 817.
 McLaughlin, M. Lyne, A. G., Keane, E. F. 2009, MNRAS, 400, 1431.
 Rea, N., McLaughlin, M. A., Gaensler, B. M. et al. 2009, ApJ 703, L41.
 Redman S. L., Rankin J. M., 2009, MNRAS, 395, 1529.
 Thompson C., Duncan R. C., 1996, ApJ, 473, 322.

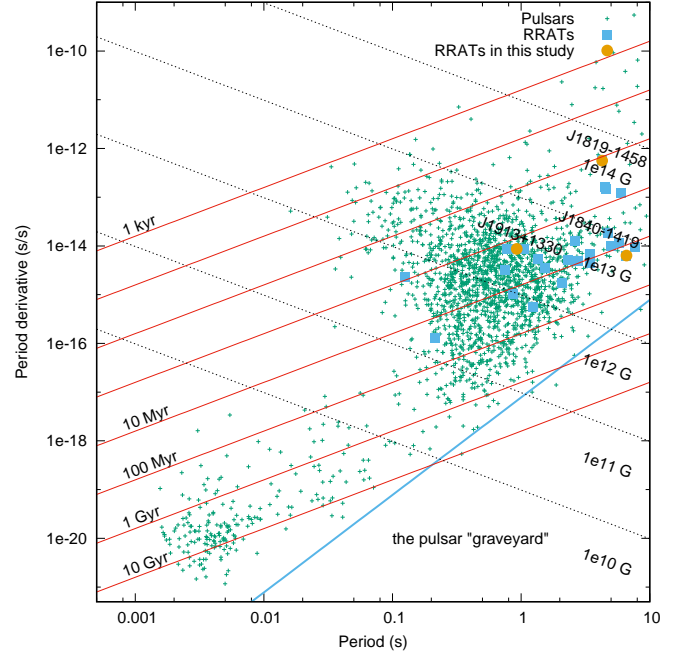


Figure A1. The $P - \dot{P}$ diagram. RRATs studied in this paper, the other pulsars and RRATs for which timing solutions are available in the ATNF Catalogue (Manchester et al. 2005) are presented. Lines of characteristic magnetic field (dotted lines), characteristic age (thin solid lines) and typical pulsar death line (Lorimer & Kramer (2004), thick solid line) are also indicated.

- Taylor, J. H., & Cordes, J. M. 1993, ApJ, 411, 674.
 Weltevrede P., Stappers B. W., 2006, ApJL, 645, 149.
 Weltevrede P., Johnston S., Espinoza C. M., 2011, MNRAS, 411, 1917.
 Weltevrede P., 2016 (<https://arxiv.org/abs/1605.06413>)
 Weisberg J. M., Nice D. J., Taylor J. H., 2010, ApJ, 722, 1030.
 Young, Weltevrede P., Stappers B. W., Lyne A. G., Kramer M., 2015, MNRAS, 449, 1495.
 Yao J. M., Manchester R. N., Wang N., 2017, ApJ, 835, 1.

APPENDIX A:

This paper has been typeset from a $\text{\TeX}/\text{\LaTeX}$ file prepared by the author.

Table A1. Variation in average burst rate for PSR J1819–1458, J1840–1419 and J1913+1330, for the epochs for which at least one pulse is detected.

RRAT name	MJD range	Burst rate (pulses/hr)
J1819–1458	55047–57436 [†]	15.5±0.5
	55100–55300	9.4±1.4
	55300–55500	6.2±1.0
	55500–55700	12.9±1.8
	55700–55900	14.2±1.5
	55900–56100	13.4±2.1
	56100–56300	22.9±2.9
	56300–56500	21.7±3.2
	56500–56700	19.2±1.9
	56700–56900	27.5±3.2
	56900–57100	16.2±2.0
	57100–57300	16.1±2.0
	57300–57500	16.3±1.5
	57500–57700	18.3±2.0
57700–57900	16.5±1.4	
57900–58000	16.5±2.0	
J1840–1419	55080–57377 [†]	24.1±0.7
	55000–55200	16.1±1.9
	55200–55400	28.3±2.6
	55400–55600	24.3±3.6
	55600–55800	29.7±2.5
	55800–56000	26.6±2.3
	56000–56200	22.1±2.5
	56200–56400	14.6±2.4
	56400–56600	27.9±2.7
	56600–56800	30.7±2.8
	56800–57000	24.5±3.4
	57000–57200	38.9±4.5
	57200–57400	18.3±2.3
	57400–57600	20.5±2.4
57600–57800	14.9±2.1	
57800–58000	16.5±4.2	
J1913+1330	55150–57400 [†]	4.7±0.2
	55200–55400	2.5±0.6
	55400–55500	2.4±0.5
	55500–55750	2.3±0.5
	55750–55900	2.1±0.5
	55900–56170	6.6±0.6
	56170–56400	6.8±0.7
	56400–56600	4.6±0.5
	56700–56900	10.9±1.2
	56900–57100	3.6±0.6
	57100–57400	4.8±0.6
	57400–57600	5.4±1.3
	57600–57800	6.6±1.3
	57800–58000	3.9±0.8
J1913+1330 (weak mode)	55942–58000	64.4±0.7 [‡]

[†] for the full range of observations

[‡] pulse emission rate considering detection of ~ 7000 pulses in weak mode over 110 hours of observations